remote sensing

Article

3-D Millimeter Wave Fast Imaging Technique Based on 2-D SISO/MIMO Array

Bo Lin [1,2,3], Yubing Yuan [1,2,3], Yicai Ji [1,2,3], Chao Li [1,2,3,*], Xiaojun Liu [1,2] and Guangyou Fang [1,2,3]

1 Aerospace Information Research Institute, Chinese Academy of Sciences, Beijing 100190, China
2 Key Laboratory of Electromagnetic Radiation and Sensing Technology, Chinese Academy of Sciences, Beijing 100190, China
3 School of Electronic, Electrical and Communication Engineering, University of Chinese Academy of Sciences, Beijing 100190, China
* Correspondence: cli@mail.ie.ac.cn; Tel.: +86-010-5888-7238

Abstract: In this article, a novel three-dimensional (3-D) imaging method based on the range decomposing algorithm (RDA) is proposed for millimeter wave imaging. We combined it with binomial theory and we derive the theoretical formulation of RDA applied to single-input–single-output (SISO)/multiple-input–multiple-output (MIMO) array; meanwhile, its computational complexity and computational error are analyzed. Compared to the classical Fourier algorithm, such as the range migration algorithm (RMA) and the phase shift migration (PSM), the proposed algorithm can replace the time-consuming interpolation and accumulation operations with reasonable approximations and transformations offering a more efficient approach, while maintaining the image quality. In addition, a method based on RDA which is applicable to the transformation between MIMO and SISO, is proposed to further enhance the processing efficiency. Proof-of-principle simulation using echo data collected from a large number of antennas, verifies that the proposed algorithm has higher efficiency. In order to better verify the feasibility of the proposed algorithm, a scanning prototype located in the millimeter wave band is designed. The experimental results of different targets demonstrate that the proposed algorithm achieves significantly higher reconstruction efficiency when compared to the traditional algorithms.

Keywords: millimeter wave fast imaging; decomposing; single-input–single-output (SISO)/multiple-input–multiple-output (MIMO) radar

Citation: Lin, B.; Yuan, Y.; Ji, Y.; Li, C.; Liu, X.; Fang, G. 3-D Millimeter Wave Fast Imaging Technique Based on 2-D SISO/MIMO Array. *Remote Sens.* **2023**, *15*, 4834. https://doi.org/10.3390/rs15194834

Academic Editors: Yin Zhang, Yulin Huang, Yachao Li and Deqing Mao

Received: 21 August 2023
Revised: 28 September 2023
Accepted: 30 September 2023
Published: 5 October 2023

1. Introduction

Millimeter wave imaging systems have attracted more and more attention due to the well penetration ability of the millimeter wave to non-metallic materials such as clothing, compared with optical and infrared radiation [1,2]. Based on the above advantages, millimeter wave radar has become a tool for many sensing applications, such as medical diagnostics, real-time security screening, etc. [3,4].

The most classical scheme based on millimeter wave image reconstruction is a 2-D monostatic array, where the transceiver antennas are distributed in the same plane following certain regulations. However, the use of this scheme leads to an extremely high number of array elements, resulting in a high system hardware cost. A combination of 1-D monostatic array and 1-D mechanical scanning can be adopted to balance the system design cost [5,6], but this will, undoubtedly, increase the imaging time significantly.

In recent years, multiple-input–multiple-out synthetic aperture radar (MIMO-SAR) has attracted more attention, which uses a combination of MIMO and mechanical scanning to further reduce system costs [7–13]. Related scholars have studied many fast imaging methods based on MIMO-SAR to speed up target 3-D reconstruction. This type of radar can achieve high-resolution imaging in azimuthal direction. Although millimeter wave imaging radars with SISO/MIMO arrays combined with mechanical scanning methods can provide some cost savings, they take a long time to acquire data once due to the presence of mechanical scanning. This is far from adequate in real-time security scenarios.

In order to achieve the best possible real-time acquisition of echo data, it is necessary to study 2-D SISO/MIMO arrays [14,15]. Due to the limitation of Nyquist's sampling law, the pitch of SISO array antenna units should be as close as possible to 1/2 wavelength; this requires a large number of antennas. At the same array aperture, the 2-D MIMO arrays can reduce the number of antennas to a large extent [1,12]. However, the data dimension of MIMO arrays is high compared to SISO arrays, so it is necessary to investigate an efficient imaging method for 2-D MIMO arrays.

The imaging problem is actually an inverse problem [16], which achieves the inversion of the target reflectivity problem by processing the received radar data. The most common imaging algorithm is the back-projection algorithm (BPA), which was first proposed by McCorkle based on the projection slice theory of computed tomography imaging [17]. In the MIMO imaging process, BPA uses an accumulation operation in each dimension to solve the reflectivity function by compensating the phase of each grid point in the target area. It is suitable for arbitrarily arranged arrays, but the computational cost is very high. In order to meet the demand for fast imaging, many scholars have proposed BPA-based fast imaging methods [18–21], but this is still a big step away from real-time imaging.

In order to reduce the cost of imaging calculations, some Fourier transform (FT) techniques are applied. The most representative algorithm is the range migration algorithm (RMA) (or ω-K algorithm) [22], which is also one of the representative algorithms for the wavenumber domain. RMA uses interpolation operation on range cells to perform migration correction, and rearrangement on azimuth to achieve 3-D reconstruction of the target [13,22–25]. The computational cost of the interpolation operation is expensive, so many scholars have combined synthetic aperture radar imaging methods with MIMO array imaging to achieve fast imaging. Tan et al. proposed a modified ω-K algorithm for 3-D reconstruction under planar MIMO geometry [26]. The algorithm used an appropriate approximation for the wavenumber domain to transform the multi-static problem into a monostatic problem in order to achieve higher computational efficiency. Some scholars have also transformed MIMO into SIMO array to solve the problem of slow imaging [27,28]. However, this method has a significant improvement in imaging speed when the number of transmitting antennas is much smaller than the number of receiving antennas. In 2020, Wang et al. proposed a modified RMA, which uses the NUFFT method to calculate the imaging results in three dimensions [29], but it still fails to break the limitation of imaging speed. The multi-static scaling algorithm (MSSA) and the chirp scaling algorithm (CSA) are relatively similar [30–34]. The wavenumber is decoupled by the phase approximation, which simplifies the imaging procedure. They achieve faster 3-D reconstruction by FT technique with a multiplication operation. In order to avoid rearrangement in MIMO-RMA, Fromenteze et al. proposed a wavenumber-spectrum deconvolution RMA [35], instead of interpolation. In MIMO array imaging, this deconvolution method can greatly improve the computational efficiency, but the phase error and side lobes are higher. In addition, some imaging methods based on compression perception have been used to deal with imaging problems [36,37]. These methods are more friendly for sparse array imaging, but they are not available for real-time imaging due to the large computation involved.

In this work, we initially develop a SISO/MIMO-based phase shift migration (PSM) algorithm, which replaces the interpolation in RMA with accumulation in the wavenumber domain. Then, the range-matching filtering operation is realized by a reasonable approximation of the range wavenumber. Finally, the 3-D reconstruction is realized by the range phase correction and IFT operation. The proposed algorithm removes the effects of interpolation and accumulation, resulting in more efficient imaging. In addition, we proposed a phase compensation method based on the similarity between MIMO and SISO range wavenumber to realize the advance rearrangement of MIMO spectrum data. This algorithm has greater computational efficiency compared to MIMO-RDA, but it comes with more constraints.

The rest of this paper is organized as follows. The theory, computational complexity, error analysis, and the derivation process of the formula are presented in Section 2. Numerical simulations and experimental validation are given in Section 3. Discussion and conclusion are given in Sections 4 and 5, respectively.

2. Theory and Formulation

2.1. The Proposed Algorithm for SISO Array Imaging

Considering the SISO imaging geometry given in Figure 1, the antenna co-ordinate is set to $(x_0, y_0, z = 0)$ while the target area is located at (x, y, z). The transmit signal is a frequency modulated continuous wave (FMCW) signal. Under this imaging scene, the corresponding frequency domain scattered echo of the target in Figure 1 can be denoted as:

$$sS(x_0, y_0, k) = \iiint_V \frac{1}{16\pi R^2} o(x, y, z) \exp[-j2(k_0 + k)R] dxdydz \quad (1)$$

where $o(x, y, z)$ is the reflectivity function of the target area, k_0 is the wavenumber corresponding to the center frequency f_0, $k = 2\pi f/c$ (f denotes the baseband sampling frequency) is the baseband wavenumber, c represents the velocity of electromagnetic wave propagation, and R denotes the distance between the target and the transceiver antenna, that is:

$$R = \sqrt{(x_0 - x)^2 + (y_0 - y)^2 + z^2} \quad (2)$$

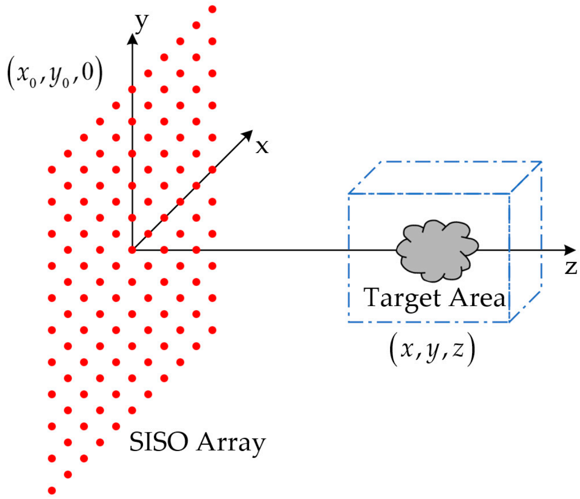

Figure 1. The scheme of the SISO imaging.

Another point to note is that the name of the function with uppercase means the wavenumber domain and with lowercase means the space domain; the former letter denotes azimuth, while the latter denotes range.

The phase information of the echo signal plays a key role in the image reconstruction while the amplitude decay factor $1/16\pi R^2$ can be ignored. Thus, (1) can be rewritten as:

$$sS(x_0, y_0, k) = \iiint_V o(x, y, z) \exp\left[-j2(k_0 + k)\sqrt{(x_0 - x)^2 + (y_0 - y)^2 + z^2}\right] dxdydz \quad (3)$$

In the SISO imaging scheme, the 'exploded fields' in free space can be obtained as follows:

$$\widetilde{U}(k_x, k_y, z, k) = \iiint_V o(x, y, z) \exp(-jk_x x - jk_y y - jk_z z) dxdydz \quad (4)$$

$$U(x, y, z, k) = \iint \widetilde{U}(k_x, k_y, z, k) \exp(jk_x x) \exp(jk_y y) dk_x dk_y \quad (5)$$

where $U(x,y,z,k)$ is the exploded field at the point (x,y,z) and $\widetilde{U}(k_x,k_y,z,k)$ is the wave spectrum of $U(x,y,z,k)$. When $t=0$, by integrating over the angular frequency, the objective function can be obtained:

$$o(x,y,z) = u(x,y,z,t)|_{t=0} = \int U(x,y,z,k)\exp[j(k_0+k)ct]d\omega|_{t=0} \tag{6}$$

Therefore, by transforming the echo signal into the 'exploded fields', the reflectivity function can be obtained by integrating the wavenumber k to achieve 3-D reconstruction of the target.

Conduct a 2-D Fourier transform (FT) to obtain the 3-D wavenumber spectrum:

$$SS(k_x,k_y,k) = \iiint_V o(x,y,z)\cdot E(k_x,k_y,k)dxdydz \tag{7}$$

$$E(k_x,k_y,k) = \iint \exp[-j2(k_0+k)R]\cdot\exp(-jk_x x_0)\cdot\exp(-jk_y y_0)dx_0dy_0 \tag{8}$$

In order to obtain sufficient support for the spatial domain, it may be necessary to zeros-fill the array in both dimensions, which means that:

$$\Delta k_x = \frac{2\pi}{N_x d_x}, \Delta k_y = \frac{2\pi}{N_y d_y} \tag{9}$$

where d_x and d_y represent the interval between the antenna cells in the x and y dimensions, respectively. We use the method of stationary phase (MSP) to solve the Fourier integral, then the wavenumber spectrum in (8) can be simplified as:

$$SS(k_x,k_y,k) = \iiint_V o(x,y,z)\exp(-jk_x x - jk_y y)\exp(-jk_z z)dxdydz \tag{10}$$

$$k_z \triangleq \sqrt{4(k_0+k)^2 - k_x^2 - k_y^2} \tag{11}$$

The formula for the SISO-based phase shift migration (PSM) can be expressed as:

$$\begin{aligned} I_{SISO-PSM}(x,y,z) &= FT_{2D}^{-1}\left\{\int_k \{FT_{2D}[sS(x_0,y_0,k)]\cdot\exp(jk_z z)\}dk\right\} \\ &= FT_{2D}^{-1}\left\{\int_k \left[SS(k_x,k_y,k)\cdot\exp(jk_z z)\right]dk\right\} \end{aligned} \tag{12}$$

The Formula (11) is the imaging principle of the PSM algorithm in the SISO scheme. By analyzing the above algorithm, it becomes apparent that the most time-consuming operation is the accumulation of the wavenumber. To improve the computational efficiency of the traditional PSM algorithm, we proposed a fast algorithm based on the frequency-range decomposing.

For a common millimeter wave near-field system, it is always considered to be satisfied $(k_0+k) \gg k_x, k_y$ and $f_0 \gg B$ (B denotes the bandwidth). This means that $k_0 \gg k$. Therefore, the range wavenumber k_z is expanded through Taylor's formula as follows:

$$\begin{aligned} k_z &= \sqrt{4(k_0+k)^2 - k_x^2 - k_y^2} \\ &\approx 2k + \left[2k_0 - \frac{k_x^2+k_y^2}{4k_0} - \frac{1}{4}\cdot\frac{\left(k_x^2+k_y^2\right)^2}{16k_0^3}\right] \\ &= 2k + \sqrt{4k_0^2 - k_x^2 - k_y^2} \end{aligned} \tag{13}$$

Thus, the term $\exp(jk_z z)$ related to range z can be decomposed as:

$$\begin{aligned} \exp(jk_z z) &= \exp[jk_z(z-z_0)]\cdot\exp(jk_z z_0) \\ &\approx \exp[j2k(z-z_0)]\cdot\exp\left[j\sqrt{4k_0^2-k_x^2-k_y^2}(z-z_0)\right]\cdot\exp(jk_z z_0) \\ &= \exp[j2k(z-z_0)]\cdot\exp[jk_{z_0}(z-z_0)]\cdot\exp(jk_z z_0) \end{aligned} \tag{14}$$

$$k_{z0} = \sqrt{4k_0^2 - k_x^2 - k_y^2} \tag{15}$$

where z_0 denotes the center plane of the region of interest (ROI). It is clear that, after decoupling, k and $2(z - z_0)$ are now an FT pair, thus, the Fourier transform method can be considered instead of the accumulation; the specific transformation process for Formula (11) is as follows:

$$\begin{aligned} o(x,y,z) &\approx FT_{2D}^{-1}\{\int_k \{SS(k_x,k_y,k)\cdot\exp[j2k(z-z_0)]\exp(jk_z z_0)\exp[jk_{z_0}(z-z_0)]\}dk\} \\ &= FT_{2D}^{-1}\left\{FT_k^{-1}[SS(k_x,k_y,k)\cdot\exp(jk_z z_0)]\cdot\exp[jk_{z_0}(z-z_0)]\right\} \\ &= FT_{2D}^{-1}\left\{FT_k^{-1}[SS_1(k_x,k_y,k)]\cdot\exp[jk_{z_0}(z-z_0)]\right\} \end{aligned} \tag{16}$$

$$SS_1(k_x,k_y,k) = SS(k_x,k_y,k)\cdot\exp(jk_z z_0) \tag{17}$$

2.2. The Proposed Algorithm for MIMO Array Imaging

The MIMO imaging regime is similar to SISO, with the difference that the processing on the wavenumber k_z is different and the spatial frequency needs to be rearranged. Consider the imaging scenario in Figure 2, the location of the transmitting and receiving antennas are located at $(x_t, y_t, 0)$ and $(x_r, y_r, 0)$, respectively. The received wave field can be obtained as follows:

$$sS(x_t,y_t,x_r,y_r,k) = \iiint_V o(x,y,z)\exp[-j(k_0+k)(R_t+R_r)]dxdydz \tag{18}$$

$$R_t = \sqrt{(x_t-x)^2 + (y_t-y)^2 + z^2} \tag{19}$$

$$R_r = \sqrt{(x_r-x)^2 + (y_r-y)^2 + z^2} \tag{20}$$

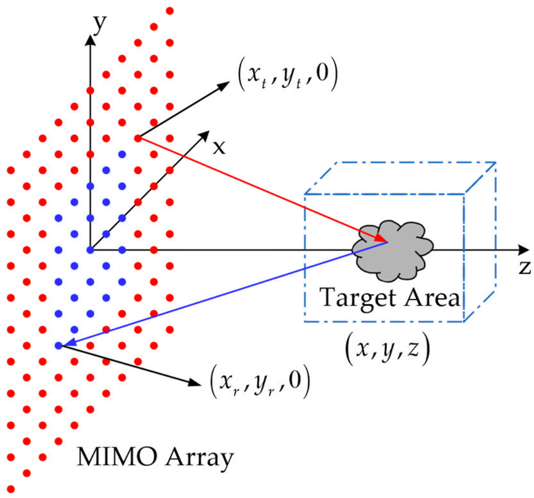

Figure 2. The scheme of the MIMO imaging.

We apply the PSM algorithm to the multi-static MIMO array, then conduct 4-D FT for Equation (16), and the 5-D spatial wavenumber spectrum of the echo signal $sS(x_t, y_t, x_r, y_r, k)$ is obtained as follows:

$$SS(k_{xt},k_{yt},k_{xr},k_{yr},k) = \iiint_V o(x,y,z)\cdot E_M(k_{xt},k_{yt},k_{xr},k_{yr},k)dxdydz \tag{21}$$

$$\begin{aligned} E_M\left(k_{xt}, k_{yt}, k_{xr}, k_{yr}, k\right) &= \iint\iint \exp[-j(k_0+k)(R_t+R_r)] \cdot \exp(-jk_{xt}x_t) \\ &\exp\left(-jk_{yt}y_t\right) \cdot \exp(-jk_{xr}x_r) \cdot \exp\left(-jk_{yr}y_r\right) dx_t dy_t dx_r dy_r \end{aligned} \quad (22)$$

We use the MSP, then we can obtain:

$$\begin{aligned} SS\left(k_{xt}, k_{yt}, k_{xr}, k_{yr}, k\right) &= \iiint_V o(x,y,z) \exp\left\{-j\left[(k_{xt}+k_{xr})x + \left(k_{yt}+k_{yr}\right)y\right]\right\} \\ &\cdot \exp(-jk_{zm}z) dxdydz \end{aligned} \quad (23)$$

$$\begin{cases} k_{xm} \triangleq k_{xt} + k_{xr} \\ k_{ym} \triangleq k_{yt} + k_{yr} \\ k_{zm} \triangleq \sqrt{(k_0+k)^2 - k_{xt}^2 - k_{yt}^2} + \sqrt{(k_0+k)^2 - k_{xr}^2 - k_{yr}^2} \end{cases} \quad (24)$$

In order to satisfy the sampling law in the azimuth direction, the number and interval of transmitters and receivers need to be satisfied:

$$N_{xt}d_{xt} = N_{xr}d_{xr}, N_{yt}d_{yt} = N_{yr}d_{yr} \quad (25)$$

Thus, the sampling interval in the spatial domain is:

$$\Delta k_{xt} = \Delta k_{xr} = \frac{2\pi}{N_{xt}d_{xt}} = \frac{2\pi}{N_{xr}d_{xr}} \quad (26)$$

$$\Delta k_{yt} = \Delta k_{yr} = \frac{2\pi}{N_{yt}d_{yt}} = \frac{2\pi}{N_{yr}d_{yr}} \quad (27)$$

Similar to the theory in the SISO regime, the PSM algorithm in the MIMO regime is formulated as follows:

$$\begin{aligned} I_{MIMO-PSM}(x,y,z) &= FT_{2D}^{-1}\left\{\left\{\int_k \{FT_{4D}[sS(x_t,y_t,x_r,y_r,k)] \cdot \exp(jk_{zm}z)\} dk\right\}_{rearrange}\right\} \\ &= FT_{2D}^{-1}\left\{\left\{\int_k \left[SS\left(k_{xt},k_{yt},k_{xr},k_{yr},k\right)\exp(jk_{zm}z)\right] dk\right\}_{rearrange}\right\} \end{aligned} \quad (28)$$

For the MIMO imaging regime, it is expected to satisfy that:

$$(k_0+k) \gg k_{xt}, k_{yt}, k_{xr}, k_{yr} \quad (29)$$

It also satisfies $k_0 \gg k$. Therefore, the range wavenumber k_{z_m} is expanded through Taylor's formula as follows:

$$\begin{aligned} k_{zm} &= \sqrt{(k_0+k)^2 - k_{xt}^2 - k_{yt}^2} + \sqrt{(k_0+k)^2 - k_{xr}^2 - k_{yr}^2} \\ &\approx 2k + \left[2k_0 - \frac{k_{xt}^2+k_{yt}^2+k_{xr}^2+k_{yr}^2}{2k_0} - \frac{k_0}{8}\left(\frac{k_{xt}^2+k_{yt}^2}{k_0^2}\right)^2 - \frac{k_0}{8}\left(\frac{k_{xr}^2+k_{yr}^2}{k_0^2}\right)^2\right] \\ &= 2k + \left(\sqrt{k_0^2 - k_{xt}^2 - k_{yt}^2} + \sqrt{k_0^2 - k_{xr}^2 - k_{yr}^2}\right) \end{aligned} \quad (30)$$

Similar to (13), the phase factor $\exp(jk_{zm}z)$ can be rewritten as:

$$\begin{aligned} \exp(jk_{zm}z) &= \exp[jk_{zm}(z-z_0)] \cdot \exp(jk_{zm}z_0) \\ &\approx \exp[j2k(z-z_0)] \cdot \exp\left[j\left(\sqrt{k_0^2-k_{xt}^2-k_{yt}^2} + \sqrt{k_0^2-k_{xr}^2-k_{yr}^2}\right)(z-z_0)\right] \cdot \exp(jk_z z_0) \\ &= \exp[j2k(z-z_0)] \cdot \exp\left[jk_{z_{m0}}(z-z_0)\right] \cdot \exp(jk_{zm}z_0) \end{aligned} \quad (31)$$

$$k_{zm0} = \sqrt{k_0^2 - k_{xt}^2 - k_{yt}^2} + \sqrt{k_0^2 - k_{xr}^2 - k_{yr}^2} \quad (32)$$

The decoupling algorithm for MIMO array is obtained as follows:

$$
\begin{aligned}
o(x,y,z) &\approx FT_{2D}^{-1}\left\{\left\{\int_k \left\{SS\left(k_{xt},k_{yt},k_{xr},k_{yr},k\right)\cdot\exp[j2k(z-z_0)]\exp(jk_{zm}z_0)\exp\left[jk_{z_{m0}}(z-z_0)\right]\right\}dk\right\}_{rearrange}\right\} \\
&= FT_{2D}^{-1}\left\{\left\{FT_k^{-1}\left[SS\left(k_{xt},k_{yt},k_{xr},k_{yr},k\right)\cdot\exp(jk_{zm}z_0)\right]\cdot\exp\left[jk_{z_{m0}}(z-z_0)\right]\right\}_{rearrange}\right\} \\
&= FT_{2D}^{-1}\left\{\left\{FT_k^{-1}\left[SS_1\left(k_{xt},k_{yt},k_{xr},k_{yr},k\right)\right]\cdot\exp\left[jk_{z_{m0}}(z-z_0)\right]\right\}_{rearrange}\right\}
\end{aligned}
\tag{33}
$$

$$
SS_1\left(k_{xt},k_{yt},k_{xr},k_{yr},k\right) = SS\left(k_{xt},k_{yt},k_{xr},k_{yr},k\right)\cdot\exp(jk_{zm}z_0) \tag{34}
$$

The proposed algorithm, which avoids the interpolation operation of the RMA and the wavenumber accumulation operation of the PSM algorithm, greatly improves the imaging efficiency. The block diagrams of the proposed algorithm in the SISO and MIMO regimes are shown in Figure 3. The analysis of the computational cost will be discussed in the Section 2.4.

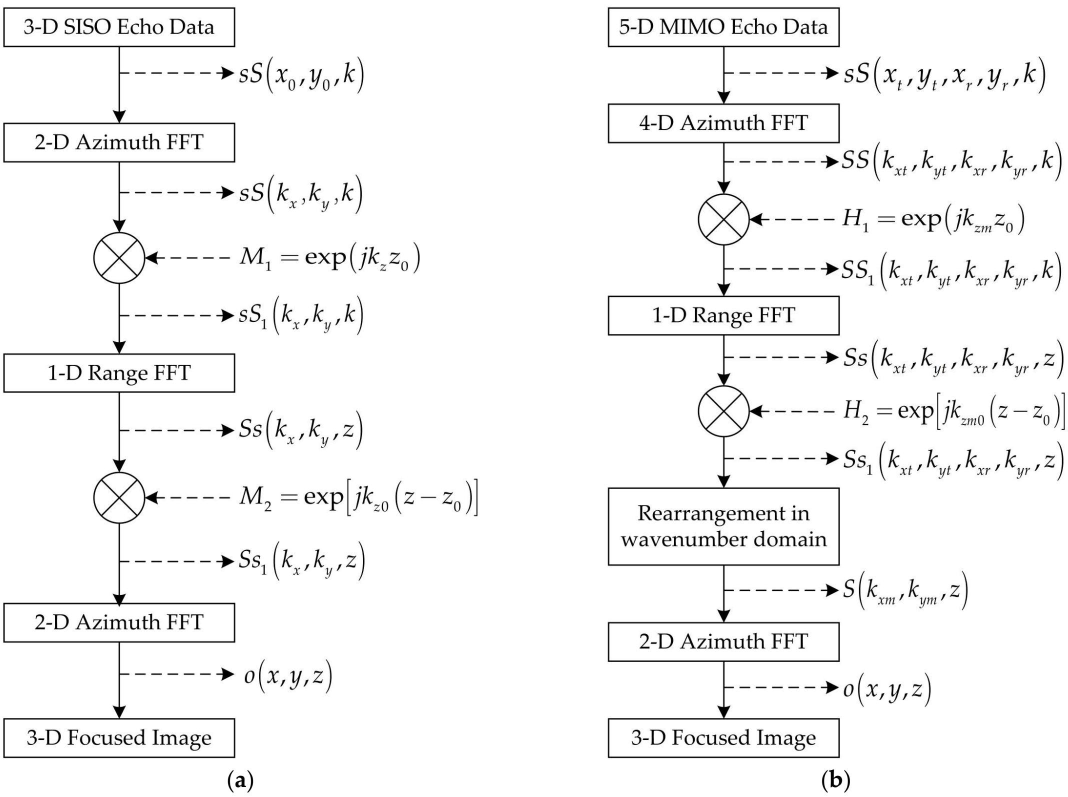

Figure 3. Block diagram of the proposed algorithm. (**a**) For SISO array. (**b**) For MIMO array.

2.3. Efficient Range Decomposing Algorithm (ERDA) Combining MIMO and SISO

The multi-dimensionality of the matrix will greatly affect the efficiency of imaging. For 2-D arrays, the computational complexity of MIMO's 5-D data is much higher than that of SISO's 3-D data. In response, a phase compensation method is proposed to transform the MIMO echo data into the echo form of SISO array by matrix rearrangement in advance. Calculating $k_{zm} - k_z$:

$$
\begin{aligned}
k_{zm} - k_z &\approx 2(k+k_0) - \frac{k_{xt}^2+k_{yt}^2+k_{xr}^2+k_{yr}^2}{2(k+k_0)} \\
&\quad -2(k+k_0) + \frac{(k_{xt}+k_{xr})^2+\left(k_{yt}+k_{yr}\right)^2}{4(k+k_0)} \\
&= -\frac{(k_{xt}-k_{xr})^2+\left(k_{yt}-k_{yr}\right)^2}{4(k+k_0)}
\end{aligned}
\tag{35}
$$

Then, the phase shift factor $\exp(jk_{zm}z)$ can be expressed as:

$$\begin{aligned} \exp(jk_{zm}z) &= \exp[j(k_{zm}-k_z)z]\exp(jk_z z) \\ &\approx \exp(jk_z z)\exp[j(k_{zm}-k_z)z_0] \end{aligned} \tag{36}$$

We substitute (31) and (32) for (24), and the target reflectance function can be transformed as:

$$I_{MIMO-PSM}(x,y,z) = FT_{2D}^{-1}\left\{\left\{\int_k \{FT_{4D}[sS(x_t,y_t,x_r,y_r,k)]\cdot\exp(jk_z z)\exp[j(k_{zm}-k_z)z_0]\}dk\right\}_{rearrange}\right\} \tag{37}$$

We define the dimensionality reduction compensation factor:

$$H_c = \exp[j(k_{zm}-k_z)z_0] \tag{38}$$

$$SS(k_{xt},k_{yt},k_{xr},k_{yr},k)\cdot H_c \overset{rearrange}{\rightarrow} SS_c(k_x,,k_y,k) \tag{39}$$

With this phase compensation, the MIMO data can be rearranged in advance to be transformed into SISO form, which, in turn, can be used for 3-D reconstruction using the imaging algorithm of the SISO array as follows:

$$I_{MIMO-PSM}(x,y,z) \underset{phase\ compensation}{\overset{rearrange}{\rightarrow}} I_{SISO-PSM}(x,y,z) \tag{40}$$

The specific algorithm flow can be seen in Figure 4.

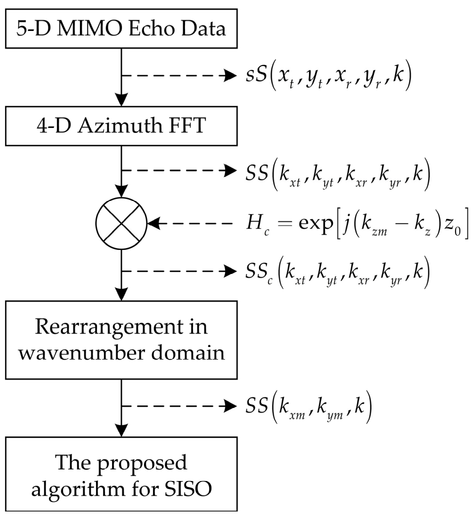

Figure 4. Block diagram of the ERDA.

2.4. Computation Complexity

Computational complexity of the proposed algorithm will be analyzed in this section. The calculation cost can be calculated by the floating-point operation (FLOP). To avoid repetitive descriptions, only the computational complexity in the MIMO regime is calculated here. According to the above imaging formulas, calculated costs can be summarized as:

$$\begin{aligned} C_{proposed} &= 5N_{xt}N_{yt}N_{xr}N_{yr}N_f\log_2\left(N_{xt}N_{yt}N_{xr}N_{yr}N_f\right) \\ &+\left(6N_f+8N_z\right)N_{xt}N_{yt}N_{xr}N_{yr} \\ &+5N_xN_yN_z\log_2(N_xN_yN_z)FLOP \end{aligned} \tag{41}$$

where N_{xt}, N_{xr} denote the number of transmitting and receiving antennas in the x-direction after zero-padding, N_{yt}, N_{yr} denote the number of transmitting and receiving antennas in the y-direction after zero-padding, N_f is the number of the sampling points of the FMCW signal, $N_x = N_{xt} + N_{xr} - 1$, $N_y = N_{yt} + N_{yr} - 1$ represent, respectively, the number of monostatic spatial wavenumbers after data rearrangement in x-direction and y-direction, and N_z is the number of samples along z-direction.

Then, we can compare the computation complexity of the BP, RMA, and PSM, which can be summarized as:

$$C_{BP} = 8N_{xt}N_{yt}N_{xr}N_{yr}N_f N_{x'} N_{y'} N_{z'} FLOP \tag{42}$$

$$\begin{aligned} C_{RMA} &= 5N_{xt}N_{yt}N_{xr}N_{yr}N_f \log_2(N_{xt}N_{yt}N_{xr}N_{yr}) \\ &+\left(8N_z + CN_f\right)N_{xt}N_{yt}N_{xr}N_{yr} \\ &+5N_xN_yN_z \log_2(N_xN_yN_z) FLOP \end{aligned} \tag{43}$$

$$\begin{aligned} C_{PSM} &= 5N_{xt}N_{yt}N_{xr}N_{yr}N_f \log_2(N_{xt}N_{yt}N_{xr}N_{yr}) \\ &+8N_zN_{xt}N_{yt}N_{xr}N_{yr} \\ &+5N_xN_yN_fN_z \log_2(N_xN_y) FLOP \end{aligned} \tag{44}$$

In comparison, the proposed algorithm has the lowest computational complexity, resulting in more efficient imaging. BP is the most computationally intensive and not suitable for real-time imaging; RMA and PSM are less computationally intensive. As a result, this paper will primarily focus on comparing the proposed algorithm with these two methods for imaging.

2.5. Error Analysis

The major phase error (PHE) in MIMO array results from the range wavenumber approximation of Formula (30). Therefore, by comparing (30) with (24), the phase error of the proposed algorithm can be defined as:

$$PHE = \max[|k_{zm} - (2k + k_{zm0})|] \cdot depth \tag{45}$$

$$depth = |z - z_0| \tag{46}$$

where *depth* is defined as the depth of the target area. It is clear that PHE has a direct correlation with relative bandwidth, squint, and target depth. When a radar system is designed, its bandwidth is fixed. Hence, this section focuses on analyzing the errors generated by the test scenarios (squint and target depth). Taking our simulation in the following section as an example, the center frequency is chosen to be 30 GHz, and the bandwidth is 6 GHz. We define the max squint as follows:

$$\sin\theta_{xt} = \frac{k_{xt\_\max}}{k_0}, \sin\theta_{yt} = \frac{k_{yt\_\max}}{k_0}, \sin\theta_{xr} = \frac{k_{xr\_\max}}{k_0}, \sin\theta_{yr} = \frac{k_{yr\_\max}}{k_0} \tag{47}$$

To simplify the analysis, the array transceiver apertures are of equal length, thus:

$$\theta_{xt} = \theta_{xr} = \theta_{yt} = \theta_{yr} = \theta \tag{48}$$

Then:

$$PHE = \left| 2k_{\max} + 2k_0\sqrt{1 - 2\sin^2\theta} - 2k_0\sqrt{\left(1 + \frac{k_{\max}}{k_0}\right) - 2\sin^2\theta} \right| \cdot depth \tag{49}$$

The phase error below 0.25π by default does not affect the image quality [16]. The relationship between PHE and target depth and squint angle is analyzed in Figure 5. According to the measurement results, the greater the target depth, the greater the PHE, and the smaller the squint, and the deeper the measurement of the target area. The analysis results verify the possibility of achieving large field imaging in the millimeter wave band, and the practicality of the algorithm is relatively high.

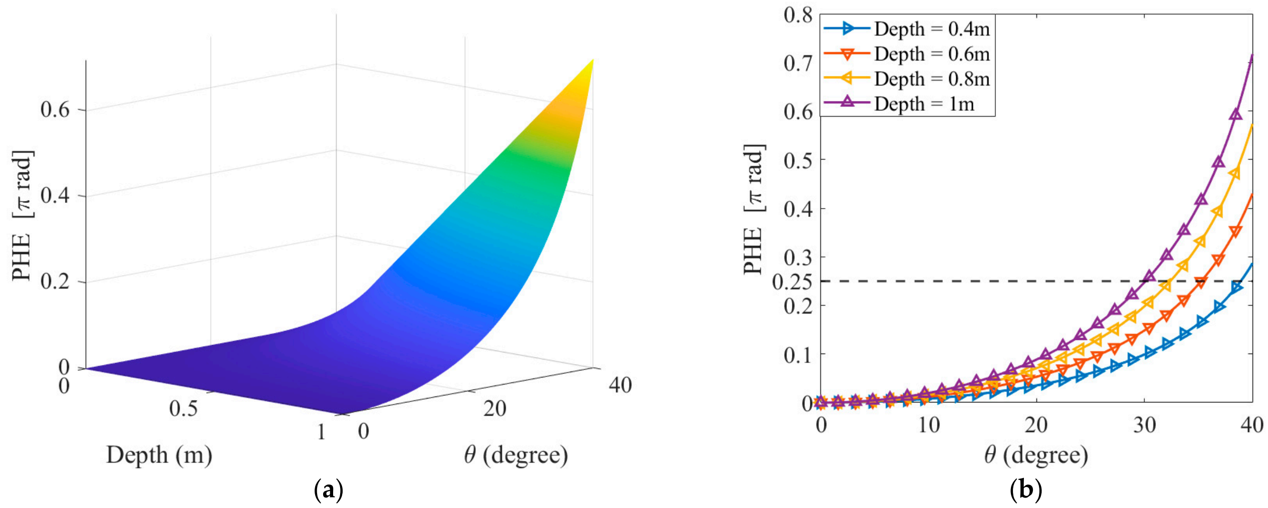

Figure 5. The variation curve of PHE with target depth and squint. (**a**) The PHE with depth and squint angle. (**b**) The PHE with squint angle at different depth.

3. Numerical Simulation and Experimental Verification

In this section, the effectiveness of the proposed algorithm will be verified by setting up a suitable millimeter wave SISO/MIMO array and simulating the Siemens star model. In addition, we set up point target simulations to analyze the specific performance of the proposed algorithm compared to the other two algorithms.

3.1. SISO/MIMO Array Simulation Experiment of Siemens Star

We use the uniform SISO array shown in Figure 6a. Furthermore, to reduce the number of required array elements, we set the center frequency to 30 GHz, the bandwidth to 6 GHz, and the number of sampling points $n_f = 21$. The number of antennas is $ns * ns$ ($ns = 41$), with an antenna spacing of 10 mm (1λ). The simulation model shown in Figure 6b is the Siemens star which is positioned at 0.5 m from the array.

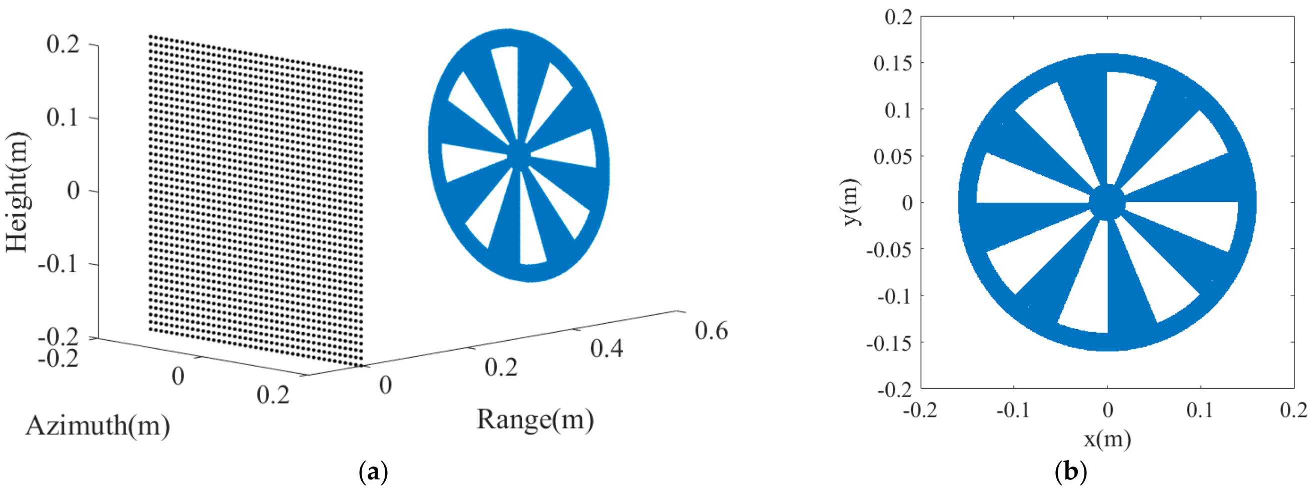

Figure 6. SISO array and siemens star model. (**a**) Location placement. (**b**) Siemens star model.

The echo signal of the SISO array is calculated using the following formula:

$$sS(x_0, y_0, k) = \sum_{i,j,l} o(x_i, y_j, z_l) \exp\left[-j2(k_0 + k)\sqrt{(x_0 - x_i)^2 + (y_0 - y_j)^2 + z_l^2}\right] \quad (50)$$

where $o(x_i, y_j, z_l)$ denotes the reflectance function of the target cell (x_i, y_j, z_l), and we set all of these to 1. Figure 7 shows the 2-D and 3-D simulation results of the SISO array for the Siemens star. The 3-D images are truncated at -10 dB. It can be found that the surface of the RMA 3-D reconstruction map is relatively rough, and the reconstruction effect is worse than the PSM and the proposed algorithm. The 2-D projections produced by all three algorithms accurately show the shape of the target. To better evaluate the focus quality of the reconstructed images, image entropy (IE) and image contrast (IC) are introduced [38]. These two parameters are, respectively, defined as follows:

$$IE = -\sum_{i,j,l} p(x_i, y_j, z_l) \ln p(x_i, y_j, z_l) \tag{51}$$

$$IC = \frac{\sqrt{E\left\{\left[|o(x_i, y_j, z_l)|^2 - E\left(|o(x_i, y_j, z_l)|^2\right)\right]^2\right\}}}{E\left(|o(x_i, y_j, z_l)|^2\right)} \tag{52}$$

where $E(\cdot)$ denotes the average operator and $p(x_i, y_j, z_l)$ denotes the power normalized image, defined as:

$$p(x_i, y_j, z_l) = \frac{|o(x_i, y_j, z_l)|^2}{\sum_{i,j,l} |o(x_i, y_j, z_l)|^2} \tag{53}$$

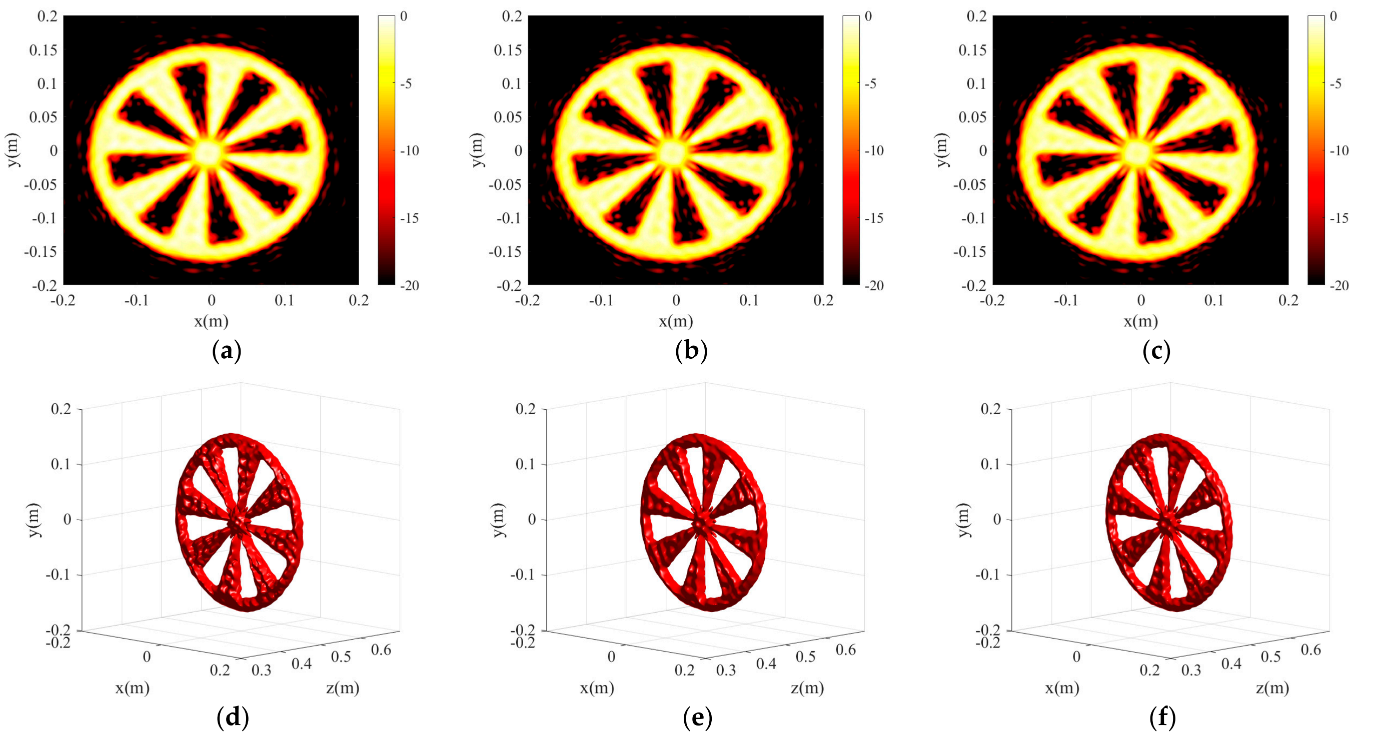

Figure 7. The simulation results for the Siemens star in SISO array scenario: (**a**,**d**) are the 2-D and 3-D projection results of RMA, (**b**,**e**) are the results of the PSM, and (**c**,**f**) are the results of the RDA.

In general, the lower the entropy, the higher the contrast, and the better the focusing quality. The simulation results for IC and IE are summarized in Table 1, and the results show that the focusing quality of the proposed algorithm is comparable to that of the other two algorithms. Thus, it can be concluded that the proposed algorithm has not compromised the quality of the image during the 3-D reconstruction process.

Table 1. SISO array reconstruction image quality comparison.

Algorithm	Image Entropy	Image Contrast
SISO-RMA	13.22	7.71
SISO-PSM	13.26	7.65
SISO-RDA (proposed)	12.97	7.99

For the Siemens star simulation of the MIMO array, we consider a MIMO array similar to Figure 6, with the same transmitting and receiving antenna positions as shown in Figure 6. Hence, it is a total of $ns \times ns \times ns \times ns \times n_f$ received data, and other parameters remain the same as those for the SISO scene. The echo signal of the MIMO array is calculated using the following formula:

$$sS(x_t, y_t, x_r, y_r, k) = \sum_{i,j,l} o(x_i, y_j, z_l) \exp[-j(k_0 + k)(R_t + R_r)] \quad (54)$$

Figure 8 shows the 2-D and 3-D simulation results of the Siemens star for the MIMO array. The 3-D images are truncated at −15 dB. All the algorithms have good reconstruction results for 2-D images. In terms of 3-D image reconstruction, RMA reconstruction has the worst effect, RDA has basically the same effect as PSM reconstruction, and the specific focusing effect comparison can be seen in Table 2. It can be seen that the difference in image reconstruction quality between RDA and PSM is almost negligible, but the imaging speed is doubled. RMA reconstructs the poorly focused images and requires the most time for reconstruction. As for ERDA, it exhibits great focus and speed, but it uses phase approximation compensation from the beginning, which limits the depth of the imaging area to some extent. But the 2-D results indicate that ERDA is significantly weaker than the other three algorithms in terms of energy at the edges, therefore, the algorithm may not work well in some cases.

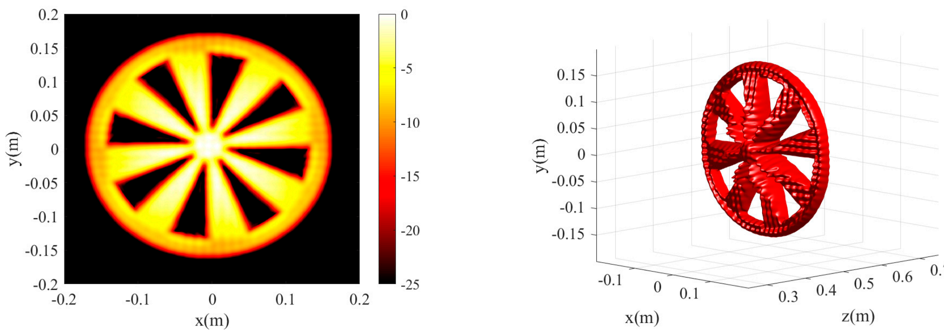

Figure 8. *Cont.*

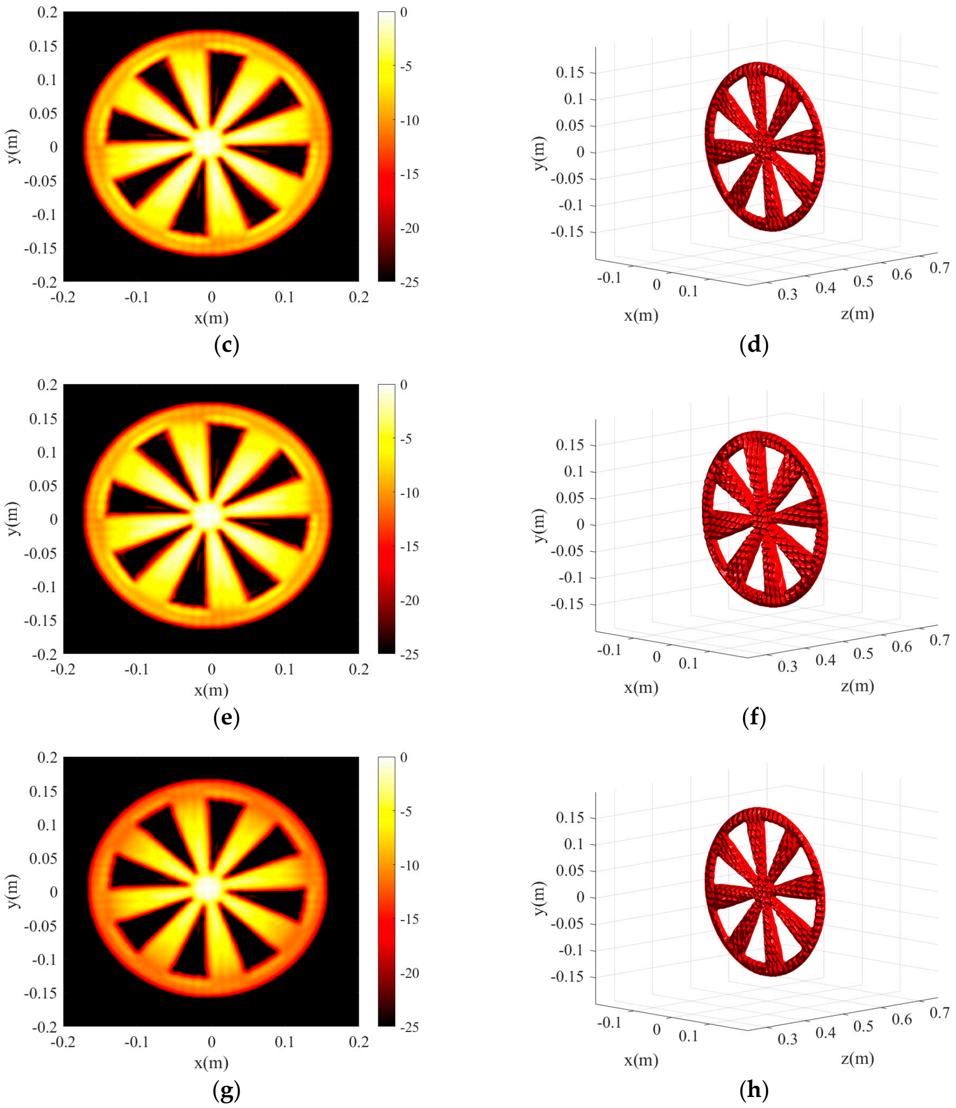

Figure 8. The simulation results for the Siemens star in MIMO array scenario: (**a**,**b**) are the 2-D and 3-D projection results of RMA, (**c**,**d**) are the results of the PSM, (**e**,**f**) are the results of the RDA, and (**g**,**h**) are the results of the ERDA.

Table 2. MIMO array reconstruction image quality comparison.

Algorithm	Image Entropy	Image Contrast	Computation Time (s)
MIMO-RMA	13.40	7.76	38.75
MIMO-PSM	12.79	8.97	18.64
MIMO-RDA (proposed)	12.83	8.92	8.99
MIMO-ERDA (proposed)	12.60	10.23	8.22

3.2. Point Target Simulation Experiment

To further analyze the performance of the imaging method, we set up 9-point targets at different locations in space under the MIMO array in the previous section for simulation. Figure 9a,c,e,g and Figure 9b,d,f,h show the 2-D and 3-D results obtained by the three algorithms, respectively. The PSM algorithm works best for the reconstruction of point targets, while RMA and the proposed algorithm work slightly worse. Then, the 1D profiles' comparison of the center point along the x-axis under the three algorithms are shown in Figure 10, and it can be found that all algorithms have a good focus effect. Table 3 gives the four algorithms for 3 dB beamwidth and the peak-to-side-lobe ratio (PSLR). The data shows that both proposed algorithms have good focusing ability on the point target compared to RMA and PSM. As for the subtle differences present, they are considered negligible within the millimeter wave band.

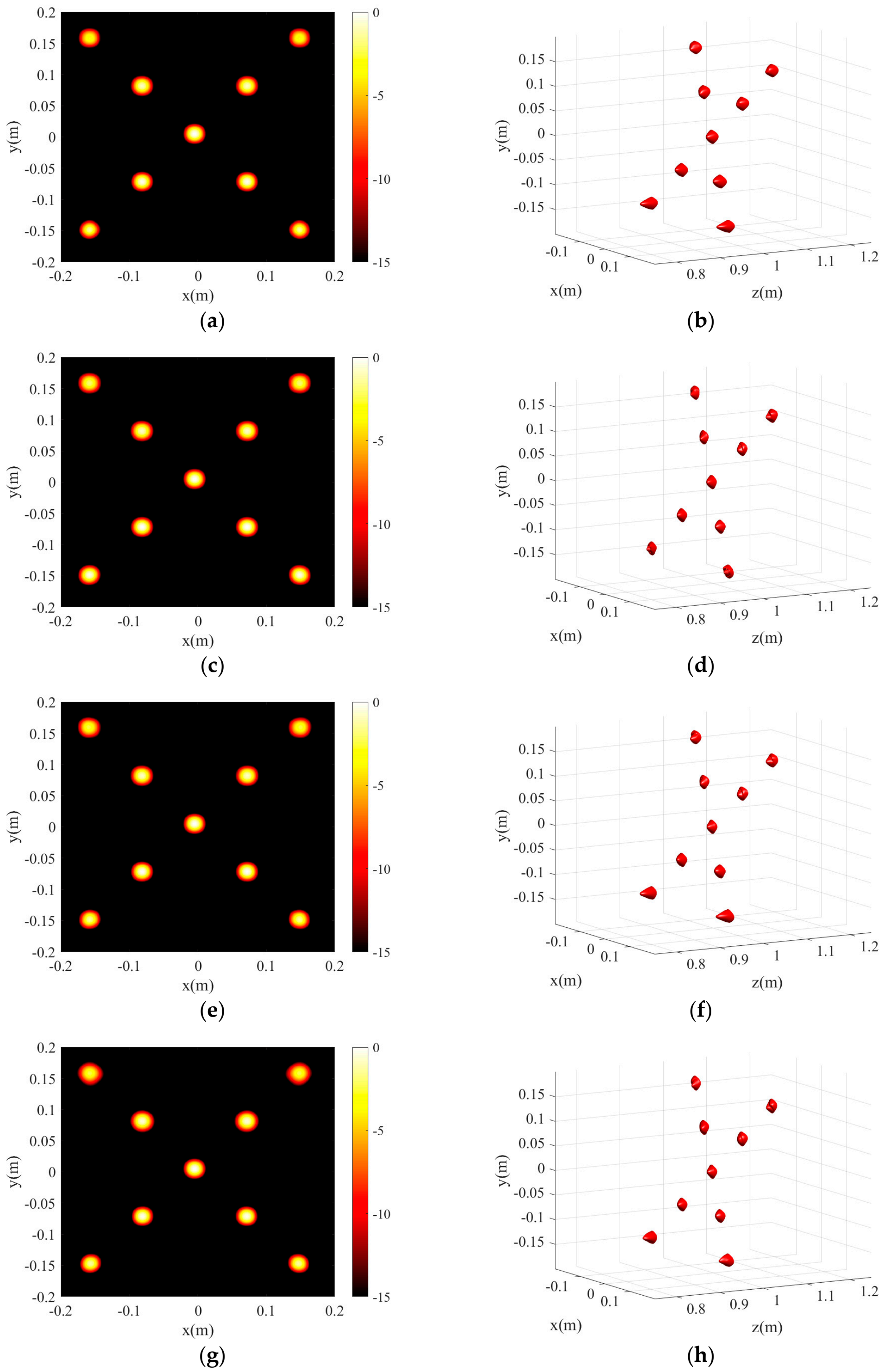

Figure 9. The simulation results of the point targets: (**a**,**b**) are the 2-D and 3-D projection results of RMA, (**c**,**d**) are the results of the PSM, (**e**,**f**) are the results of the proposed algorithm, and (**g**,**h**) are the results of the ERDA.

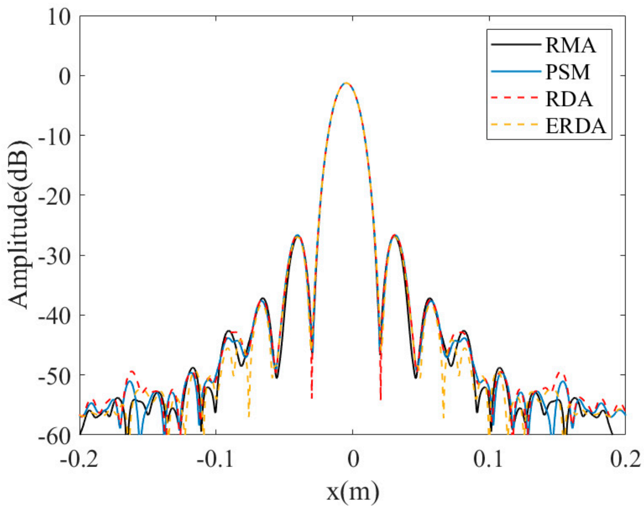

Figure 10. The 1-D profile along x-axis of the center point target under −60 dB.

Table 3. 3-dB beamwidth and PSLR.

Algorithms	3-dB Beamwidth (cm)	PSLR (dB)
MIMO-RMA	1.230	−25.61
MIMO-PSM	1.237	−25.38
MIMO-RDA (proposed)	1.236	−25.34
MIMO-ERDA (proposed)	1.234	−25.67

3.3. Comparison of Algorithms in SISO Array Imaging Experiment

The above simulation experiments verify the effectiveness of the proposed algorithm, and the proposed ERDA successfully realizes the conversion of the algorithm between MIMO and SISO. In this section, we focus on validating the proposed algorithm using the developed prototype imaging system prototype as shown in Figure 11. The echo data are obtained through a transmitter and a receiver of the prototype, scanning on a 2-D plane. With a center frequency of 200 GHz and a signal bandwidth of 30 GHz, experiments are conducted on a metal target and a human model with pistol, respectively. The optical picture of the target can be seen in Figure 12. For the metal target, the canning points (interval) in the azimuth and height are 300 (1.9 mm) and 300 (1 mm). As for the human model, these parameters are 300 (2 mm) and 300 (2 mm). The number of the signal sampling points is 200.

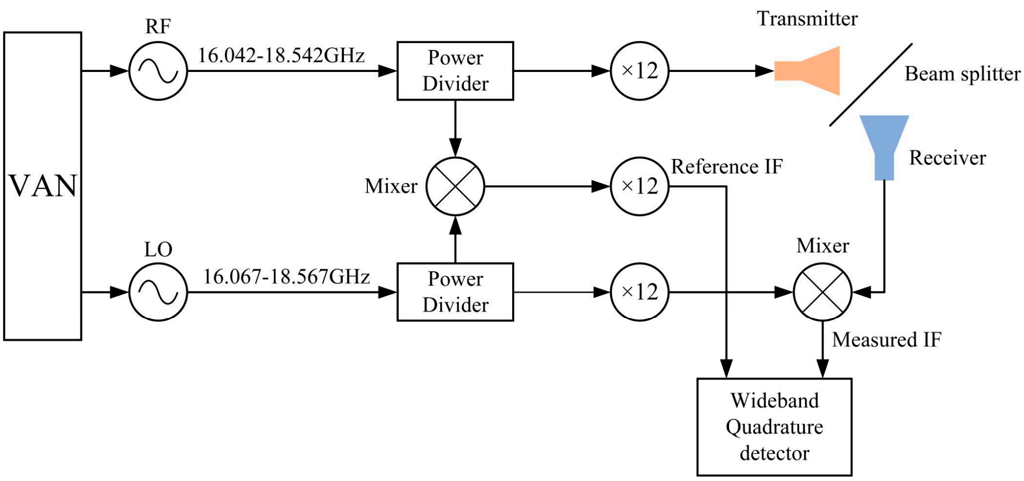

Figure 11. The schematic of the experimental prototype.

(**a**) (**b**)

Figure 12. Optical picture of targets. (**a**) Metal target. (**b**) Human model with pistol.

From the theoretical derivation in Section 2, it can be seen that the algorithmic flow of MIMO and SISO is basically the same, and especially note that our proposed ERDA can transform the MIMO form into the SISO form. Due to the limitation of experimental equipment, we only verify the algorithm in SISO form.

As seen in the experimental results presented in Figures 13 and 14, all the algorithms (RMA, PSM, and RDA) achieve excellent reconstruction of the target. The metal bars on the metal target are distinguished in the reconstruction results, and the pistol carried on the human model can be easily seen in the 2-D and the 3-D image. Tables 4 and 5 demonstrate the image focusing quality and the processing time of the algorithms, and it can be seen that there is very little difference in the focusing quality of the algorithms, but the proposed algorithm has obvious efficiency advantages.

Table 4. Image quality comparison of metal target.

Algorithm	Image Entropy	Image Contrast	Computation Time (s)
SISO-RMA	13.62	31.44	2.54
SISO-PSM	13.78	30.33	17.2
SISO-RDA (proposed)	13.74	30.75	0.89

Table 5. Image quality comparison of human model with pistol.

Algorithm	Image Entropy	Image Contrast	Computation Time (s)
SISO-RMA	13.07	50.42	3.89
SISO-PSM	13.11	50.52	30.26
SISO-RDA (proposed)	13.15	49.49	1.03

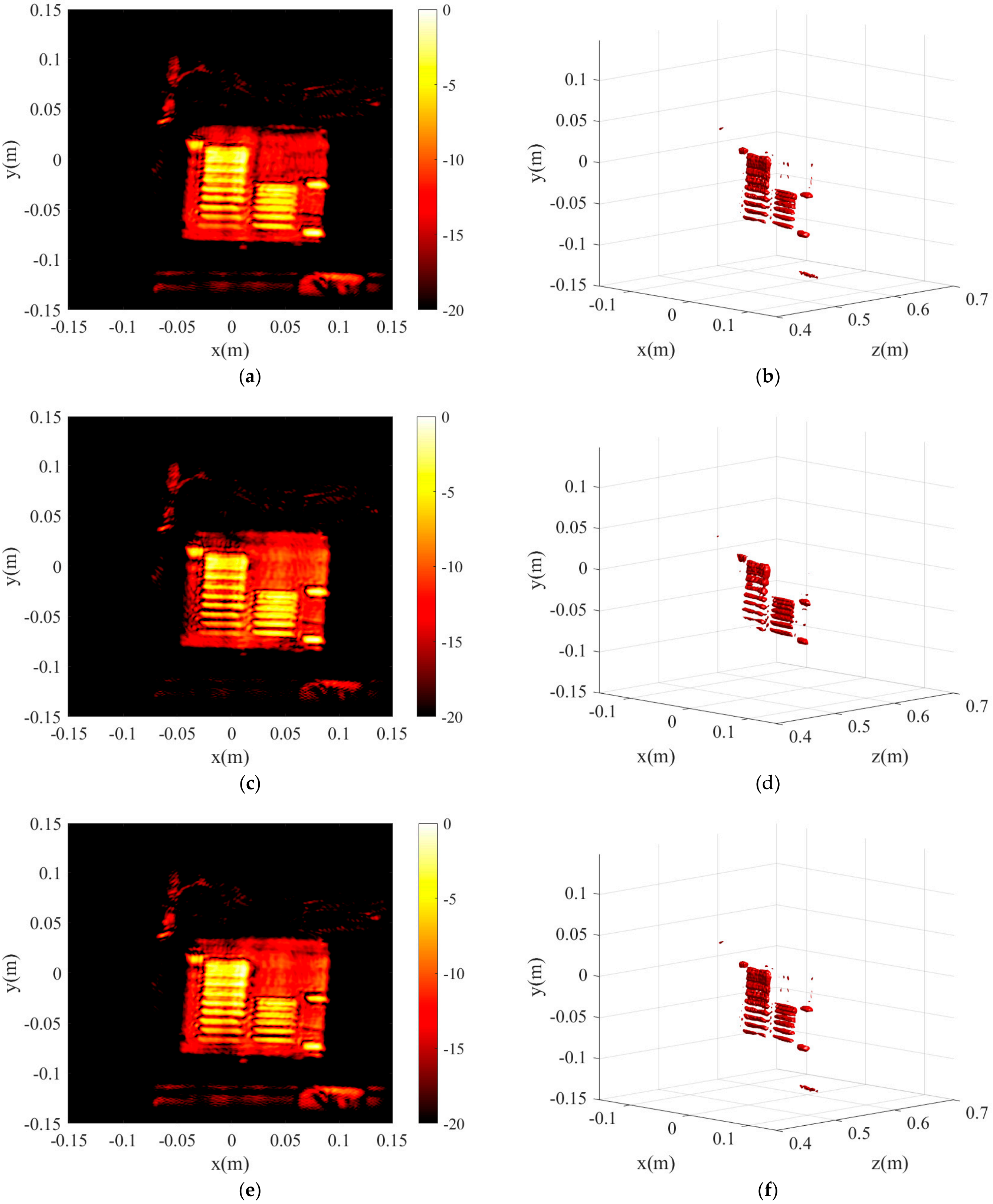

Figure 13. The results of the metal target: (**a**,**b**) are the 2-D and 3-D (−15 dB) projection results of RMA, (**c**,**d**) are the results of the PSM, and (**e**,**f**) are the results of the proposed algorithm.

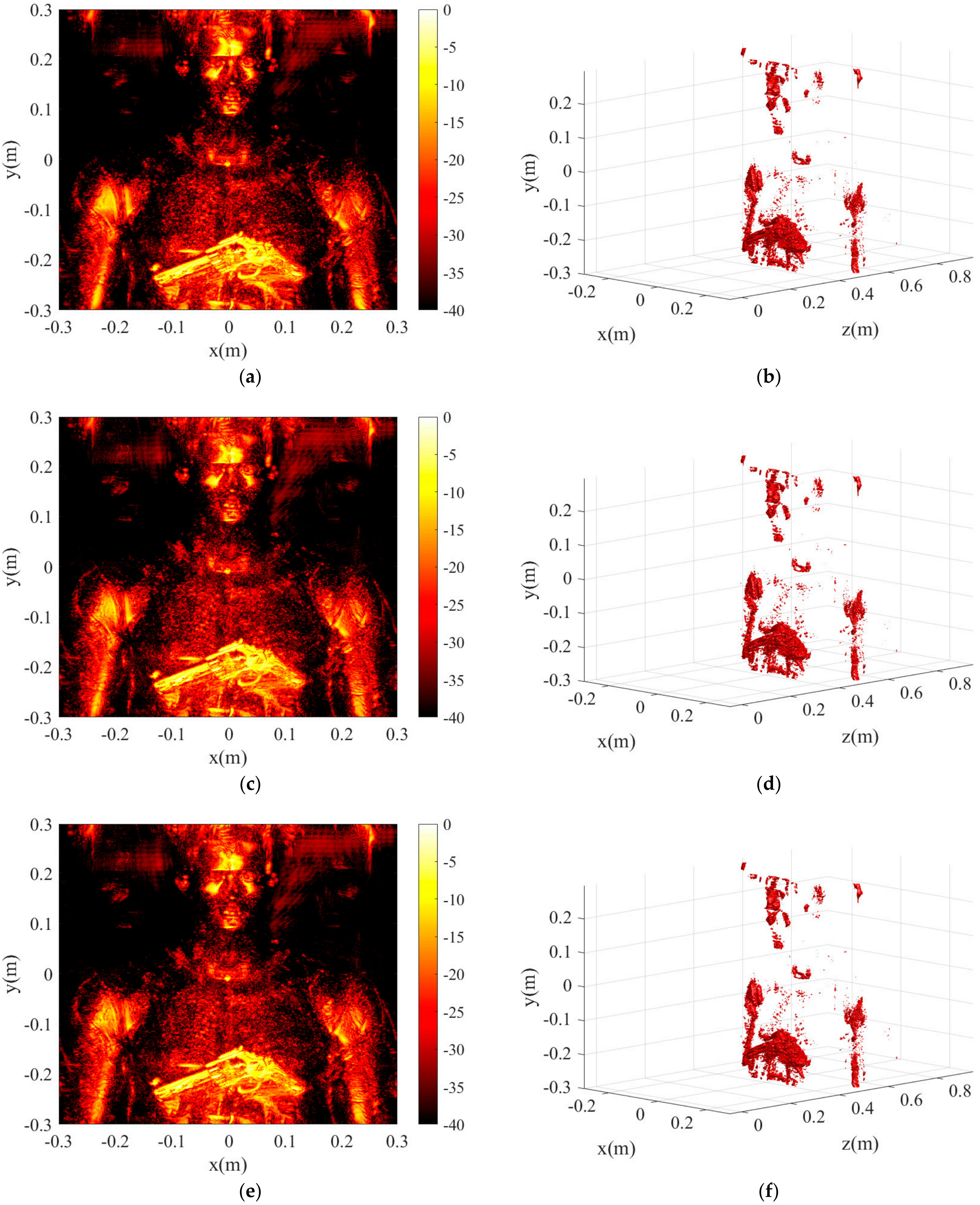

Figure 14. The results of the human model with the pistol: (**a**,**b**) are the 2-D and 3-D (−25 dB) projection results of RMA, (**c**,**d**) are the results of the PSM, and (**e**,**f**) are the results of the proposed algorithm.

4. Discussion

For the 3-D fast imaging algorithm applicable to 2-D sparse SISO/MIMO array proposed in this paper, we, firstly, performed a simulation of the Siemens star model using SISO array in Section 3, and, then, validated the two imaging algorithms applicable to MIMO array. In order to further validate the algorithms, we developed a prototype to conduct experiments on the metal target and the human model with a pistol in Section 3.3, and the experiments' results coincided with the simulation results in Section 3.

In this paper, we employed the reconstructed image, IC, IE, and imaging time as the metrics to evaluate the performance of the algorithm, respectively. Simulation and experimental results indicated that there may be differences in imaging speed between RMA and PSM due to different scenes and parameters. But RDA achieves 3-D reconstruction with greater efficiency without compromising image quality when compared to RMA and PSM in any scenario.

The proposed ERDA allows the MIMO echo data to be rearranged in advance to fulfill the form of SISO data, which has a higher efficiency than RDA. However, due to the range of approximation used, this leads to a prerequisite for the use of ERDA: to be as precise as possible about the range between the target and the array. This is reflected in the derivation presented in Section 2.3. The initial phase compensation contains range information about the location of the target plane, and it is necessary to accurately obtain information about the target range. This indicts more stringent constraints on the utilization of ERDA.

Due to the advantage of the high efficiency of the proposed algorithms, they can be considered for applications in real-time imaging of SISO/MIMO arrays with massive antennas to meet the demand of real-time security screening. Figure 15 shows the side view of the human model reconstructed by RDA, from which the gun on the chest can be visualized. In conclusion, it is necessary to choose RDA or ERDA for rapid imaging which depends on the needs of the screening scenario. Another consideration to keep in mind is: since the characteristics of the array and the scattering ability of the target are different, it is reasonable to adjust the dynamic range of the reconstructed image according to the needs of the array and the imaging scene. This is the reason why different dynamic ranges are selected in different simulations and different experiments.

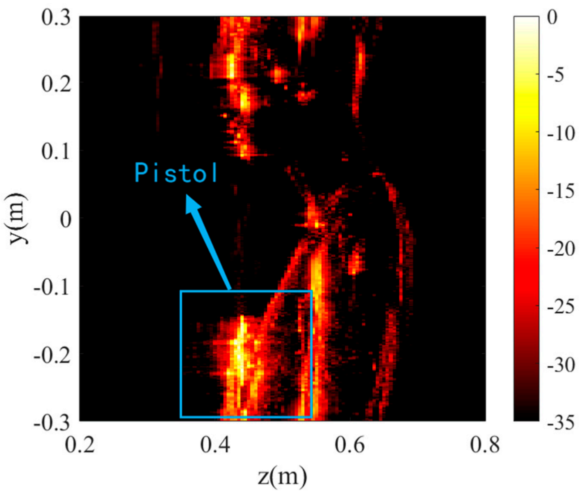

Figure 15. The side view of the human model with the pistol.

5. Conclusions

In this paper, a range decoupling algorithm based on millimeter SISO/MIMO array is proposed. By decomposing the range wavenumber with a reasonable approximation, 3-D reconstruction can be achieved using only Fourier transform and matrix multiplication. Comparing the computational complexity of the proposed algorithm with RMA and PSM, it exhibits the lowest computation load. In addition, based on the wavenumber relationship between SISO and MIMO echo signals, the conversion from MIMO to SISO is realized by phase compensation; then, the reconstruction can be realized by applying the algorithm in the SISO regime. The proposed algorithms have higher imaging efficiency without compromising the image quality, compared to the traditional algorithms. Based on the self-designed imaging prototype system, the effectiveness of the proposed algorithm is demonstrated by producing imaging results of various targets. The main contribution of this paper is to propose efficient imaging algorithms applied to millimeter wave SISO/MIMO arrays, which are, theoretically, applicable to a wide range of imaging scenarios.

Author Contributions: B.L. performed the theoretical arguments, conducted the experiments, and processed and wrote the manuscript. C.L. designed the imaging system and revised the manuscript together with Y.J. Y.Y. helped examine the manuscript. X.L. and G.F. provided the experiment equipment and funds for the research. All authors have read and agreed to the published version of the manuscript.

Funding: This work was funded by the Beijing Municipal Natural Science Foundation under grant number L223007, by the Key Area Research and Development Program of the Guangdong Province under grant number 2020B0101110001, by the National Natural Science Foundation of China under grant numbers 61988102 and 61731020, by the National Key Research and Development Program of China under grant number 2017YFA0701004, by the Project of Equipment Pre-Research under grant number WJ2019G00019, and by the Key Program of Scientific and Technological Innovation from the Chinese Academy of Sciences under grant number KGFZD-135-18-029.

Data Availability Statement: No new data were created or analyzed in this study. Data sharing is not applicable to this article.

Acknowledgments: The authors would like to thank the editors and reviewers for their efforts to help the publication of this work.

Conflicts of Interest: The authors declare no conflict of interest.

References

1. Cheng, B.; Cui, Z.; Lu, B.; Qin, Y.; Liu, Q.; Chen, P.; He, Y.; Jiang, J.; He, X.; Deng, X.; et al. 340-GHz 3-D Imaging Radar With 4Tx-16Rx MIMO Array. *IEEE Trans. Terahertz Sci. Technol.* **2018**, *8*, 509–519. [CrossRef]
2. Zhong, H.; Xu, J.; Xie, X.; Yuan, T.; Reightler, R.; Madaras, E.; Zhang, X.C. Nondestructive defect identification with terahertz time-of-flight tomography. *IEEE Sens. J.* **2005**, *5*, 203–208. [CrossRef]
3. Meo, S.D.; Espín-López, P.F.; Martellosio, A.; Pasian, M.; Matrone, G.; Bozzi, M.; Magenes, G.; Mazzanti, A.; Perregrini, L.; Svelto, F.; et al. On the feasibility of breast cancer imaging systems at millimeter-waves frequencies. *IEEE Trans. Microw. Theory Tech.* **2017**, *65*, 1795–1806. [CrossRef]
4. Sheen, D.M.; Mcmakin, D.L.; Hall, T.E.; Severtsen, R.H. Active millimeter-wave standoff and portal imaging techniques for personnel screening. In Proceedings of the 2009 IEEE Conference on Technologies for Homeland Security, Boston, MA, USA, 11–12 May 2009; pp. 440–447.
5. Sheen, D.M.; Mcmakin, D.L.; Hall, T.E. Three-dimensional millimeter-wave imaging for concealed weapon detection. *IEEE Trans. Microw. Theory Techn.* **2001**, *9*, 1581–1592. [CrossRef]
6. Sheen, D.M.; Collins, H.D.; Hall, T.E.; McMakin, D.L.; Gribble, R.P.; Severtsen, R.H.; Prince, J.M.; Reid, L.D. Real-Time Wideband Holographic Surveillance System. U.S. Patent 5,557,283, 17 September 1996.
7. Zhuge, X.; Yarovoy, A.G. A sparse aperture MIMO-SAR-based UWB imaging system for concealed weapon detection. *IEEE Trans. Geosci. Remote Sens.* **2011**, *1*, 509–518. [CrossRef]
8. Gumbmann, F.; Schmidt, L. Millimeter-wave imaging with optimized sparse periodic array for short-range applications. *IEEE Trans. Geosci. Remote Sens.* **2011**, *10*, 3629–3638. [CrossRef]
9. Yang, G.; Li, C.; Wu, S.; Liu, X.; Fang, G. MIMO-SAR 3-D Imaging Based on Range Wavenumber Decomposing. *IEEE Sens. J.* **2021**, *21*, 24309–24317. [CrossRef]
10. Zhu, R.; Zhou, J.; Jiang, G.; Fu, Q. Range Migration Algorithm for Near-Field MIMO-SAR Imaging. *IEEE Geosci. Remote Sens. Lett.* **2017**, *14*, 2280–2284. [CrossRef]
11. Fan, B.; Gao, J.; Li, H.; Jiang, Z.; He, Y. Near-Field 3-D SAR Imaging Using a Scanning Linear MIMO Array with Arbitrary Topologies. *IEEE Access.* **2020**, *8*, 6782–6791. [CrossRef]
12. Bleh, D.; Rosch, M.; Kuri, M.; Dyck, A.; Tessmann, A.; Leuther, A.; Wagner, S.; Weismann-Thaden, B.; Stulz, H.P.; Zink, M.; et al. W-Band Time-Domain Multiplexing FMCW MIMO Radar for Far-Field 3-D Imaging. *IEEE Trans. Microw. Theory Tech.* **2017**, *65*, 3474–3484. [CrossRef]

13. Gao, J.; Qin, Y.; Deng, B.; Wang, H.; Li, X. Novel effificient 3-D shortrange imaging algorithms for a scanning 1D-MIMO array. *IEEE Trans. Image Process.* **2018**, *27*, 3631–3643. [CrossRef] [PubMed]
14. Ahmed, S.S.; Schiessl, A.; Schmidt, L.-P. A novel fully electronic active real-time imager based on a planar multistatic sparse array. *IEEE Trans. Microw. Theory Techn.* **2011**, *12*, 3567–3576. [CrossRef]
15. Ahmed, S.S.; Genghammer, A.; Schiessl, A.; Schmidt, L. Fully electronic *E*-band personnel imager of 2m2 aperture based on a multistatic architecture. *IEEE Trans. Microw. Theory Techn.* **2013**, *1*, 651–657. [CrossRef]
16. Cumming, I.G.; Wong, F.H. *Digital Signal Processing of Synthetic Aperture Radar Data: Algorithms and Implementation*; Artech House: Norwood, MA, USA, 2005.
17. Mccorkle, J.W. Focusing of synthetic aperture ultra wideband data. In Proceedings of the IEEE 1991 International Conference on Systems Engineering, Dayton, OH, USA, 1–3 August 1991; Volume 8, pp. 1–5.
18. Mccorkle, J.W.; Rofheart, M. Order N2 log(N) backprojector algorithm for focusing wide-angle wide-bandwidth arbitrary-motion synthetic aperture radar. *Proc. SPIE Radar Sensor Technol.* **1996**, *6*, 25–36.
19. Boag, A.; Bresler, Y.; Michielssen, E. A multilevel domain decomposition algorithm for fast O(N2/logN) reprojection of tomographic images. *IEEE Trans. Image Process.* **2000**, *9*, 633–636. [CrossRef]
20. Ponce, O.; Prats-Iraola, P.; Pinheiro, M.; Rodriguez-Cassola, M.; Scheiber, R.; Reigber, A.; Moreira, A. Fully polarimetric high-resolution 3-D imaging with circular SAR at L-band. *IEEE Trans. Geosci. Remote Sens.* **2014**, *6*, 3074–3090. [CrossRef]
21. Yegulalp, A.F. Fast backprojection algorithm for synthetic aperture radar. *Proc. IEEE Radar Conf. Radar Next Millennium* **1999**, *4*, 60–65.
22. Zhuge, X.; Yarovoy, A.G. Three-dimensional near-field MIMO array imaging using range migration techniques. *IEEE Trans. Image Process.* **2012**, *6*, 3026–3033. [CrossRef]
23. Wu, S.; Wang, H.; Li, C.; Liu, X.; Fang, G. A modified omega-K algorithm for near-fifield single-frequency MIMO-arc-array-based azimuth imaging. *IEEE Trans. Antennas Propag.* **2021**, *8*, 4909–4922. [CrossRef]
24. Wang, Z.; Guo, Q.; Tian, X.; Chang, T.; Cui, H.-L. Near-field 3-D millimeter-wave imaging using MIMO RMA with range compensation. *IEEE Trans. Microw. Theory Techn.* **2019**, *3*, 1157–1166. [CrossRef]
25. Guo, Q.; Zhang, X.; Chang, T.; Cui, H.-L.; Tian, X. Three dimensional bistatic array imaging using range migration algorithm. *Electron. Lett.* **2017**, *2*, 193–194. [CrossRef]
26. Tan, K.; Wu, S.; Liu, X.; Fang, G. A modified omega-K algorithm for near-field MIMO array-based 3-D reconstruction. *IEEE Geosci. Remote Sens. Lett. Oct.* **2018**, *10*, 1555–1559. [CrossRef]
27. Yang, G.; Li, C.; Gao, H.; Fang, G. Phase shift migration with SIMO superposition for MIMO-side looking imaging at terahertz band. *IEEE Access* **2020**, *8*, 208418–208426. [CrossRef]
28. Tan, K.; Wu, S.; Liu, X.; Fang, G. Omega-K algorithm for near-field 3-D image reconstruction based on planar SIMO/MIMO array. *IEEE Trans. Geosci. Remote Sens.* **2019**, *4*, 2381–2394. [CrossRef]
29. Wang, J.; Aubry, P.; Yarovoy, A. 3-D short-range imaging with irregular MIMO arrays using NUFFT-based range migration algorithm. *IEEE Trans. Geosci. Remote Sens.* **2020**, *7*, 4730–4732. [CrossRef]
30. Tan, K.; Chen, X.; Wu, S.; Fang, G. Efficient frequency scaling algorithm for short-range 3-D holographic imaging based on a scanning MIMO array. *IEEE Trans. Microw. Theory Techn.* **2020**, *9*, 3885–3897. [CrossRef]
31. Tan, K.; Chen, X. Fast 3-D image reconstruction on nonregular UWB sparse MIMO planar array using scaling techniques. *IEEE Trans. Microw. Theory Techn.* **2021**, *1*, 222–234. [CrossRef]
32. Wang, C.; Zhang, Q.; Hu, J.; Li, C.; Shi, S.; Fang, G. An efficient algorithm based on CSA for THz stepped-frequency SAR imaging. *IEEE Geosci. Remote Sens. Lett.* **2022**, *19*, 1–5. [CrossRef]
33. Wang, C.; Zhang, Q.; Hu, J.; Shi, S.; Li, C.; Cheng, W.; Fang, G. An Efficient Algorithm Based on Frequency Scaling for THz Stepped-Frequency SAR Imaging. *IEEE Trans. Geosci. Remote Sens.* **2022**, *60*, 1–15. [CrossRef]
34. Zhang, W.; Ji, Y.; Shao, W.; Lin, B.; Li, C.; Fang, G. A Fast 3-D Chirp Scaling Imaging Technique for Millimeter-Wave Near-Field Imaging. *IEEE Trans. Microw. Theory Techn.* **2023**, *2*, 827–841. [CrossRef]
35. Fromenteze, T.; Yurduseven, O.; Berland, F.; Decroze, C.; Smith, D.R.; Yarovoy, A.G. A transverse spectrum deconvolution technique for MIMO short-range Fourier imaging. *IEEE Trans. Geosci. Remote Sens.* **2019**, *9*, 6311–6324. [CrossRef]
36. Alvarez, Y.; Rodriguez-Vaqueiro, Y.; Gonzalez-Valdes, B.; Rappaport, C.; Las-Heras, F.; Martinez-Lorenzo, J. Three dimensional compressed sensing-based millimeter-wave imaging. *IEEE Trans. Antennas Propag.* **2015**, *12*, 2868–5873. [CrossRef]
37. Li, S.; Zhao, G.; Sun, H.; Amin, M. Compressive sensing imaging of 3-D object by a holographic algorithm. *IEEE Trans. Antennas Propag.* **2018**, *12*, 7295–7304. [CrossRef]
38. Zhu, R.; Zhou, J.; Chen, B.; Fu, Q.; Jiang, G. Sequential frequency domain imaging algorithm for near-field MIMO-SAR with arbitrary scanning paths. *IEEE J. Sel. Topics Appl. Earth Observ. Remote Sens.* **2019**, *8*, 2967–2975. [CrossRef]